CrossMark

Wave observation in the marginal ice zone with the TerraSAR-X satellite

Claus Gebhardt[1] · Jean-Raymond Bidlot[2] · Johannes Gemmrich[3] · Susanne Lehner[1] ·
Andrey Pleskachevsky[1] · Wolfgang Rosenthal[1]

Abstract This article investigates the penetration of ocean waves into the marginal ice zone (MIZ), observed by satellite, and likewise provides a basis for the future cross-validation of respective models. To this end, synthetic aperture radar images from the TerraSAR-X satellite (TS-X) and numerical simulations of the European Centre for Medium-Range Weather Forecasts (ECMWF) are used. The focus is an event of swell waves, developed during a storm passage in the Atlantic, penetrating deeply into the MIZ off the coast of Eastern Greenland in February 2013. The TS-X scene which is the basis for this investigation extends from the ice-free open ocean to solid ice. The variation of the peak wavelength is analysed and potential sources of variability are discussed. We find an increase in wavelength which is consistent with the spatial dispersion of deep water waves, even within the ice-covered region.

✉ Claus Gebhardt
  Claus.Gebhardt@dlr.de

[1] German Aerospace Center (DLR), Remote Sensing Technology Institute, Maritime Safety and Security Lab, Bremen, Germany

[2] European Centre for Medium-Range Weather Forecasts (ECMWF), Earth Modelling Section, Coupled Processes, Reading, UK

[3] Department of Physics & Astronomy, University of Victoria, Victoria, British Columbia, Canada

1 Introduction

The interaction of water waves with sea ice has various implications involving interdisciplinary fields of research. The range of influence extends from enhanced air-sea exchange processes and upper ocean mixing to land erosion, only to name a few. This leads to the issue of potential feedback processes between waves and ice, e.g. the break-up of ice by waves leads to a larger water/air interface. This, in turn, may be connected to enhanced absorption of solar radiation and less ice formation. All this is of particular relevance in the context of a changing ocean wave and sea ice climate.

Over the last few decades, the propagation of ocean waves into the marginal ice zone (MIZ) was investigated by in situ measurements in field campaigns, by remote sensing methods, and by laboratory experiments using ice tanks. These studies ranged from waves in frazil and pancake ice to waves encountering ice floes. Based on different theoretical approaches, models were developed to describe the wave ice interaction. For details, see Doble et al. (2015), Doble and Bidlot (2013), and Kohout et al. (2014), the review papers of Squire (2007) and Squire et al. (1995), and references therein.

The potential of spaceborne synthetic aperture radar (SAR) instruments to reveal the modulation of wave parameters in in the MIZ was already pointed out by Wadhams et al. (1986). Subsequently, notable insight into ocean waves in sea ice was gained from SAR satellite images. Later studies such as Schulz-Stellenfleth and Lehner (2002), Wadhams et al. (2002), and Wadhams et al. (2004) address

the attenuation of the sea state in ice with the objective of retrieving sea ice parameters from the wave patterns imaged by SAR. Altogether, the aforementioned publications involve case studies on different conditions of the sea state in the MIZ ranging from local wind sea to long swell waves. Different ice types including frazil/grease ice, pancake ice, brash ice and ice floes are encountered. On the basis of a series of Sentinel-1A SAR observations in wave mode, SAR-based results on the significant wave height in sea ice were reported in the recent study of Ardhuin et al. (2015). Different approaches of significant wave height retrieval were tested, and the role of non-linear imaging effects was pointed out.

Here, we analyse high-resolution TerraSAR-X (TS-X) images of a complex wave field penetrating into the MIZ off the coast of Eastern Greenland in February 2013. The MIZ
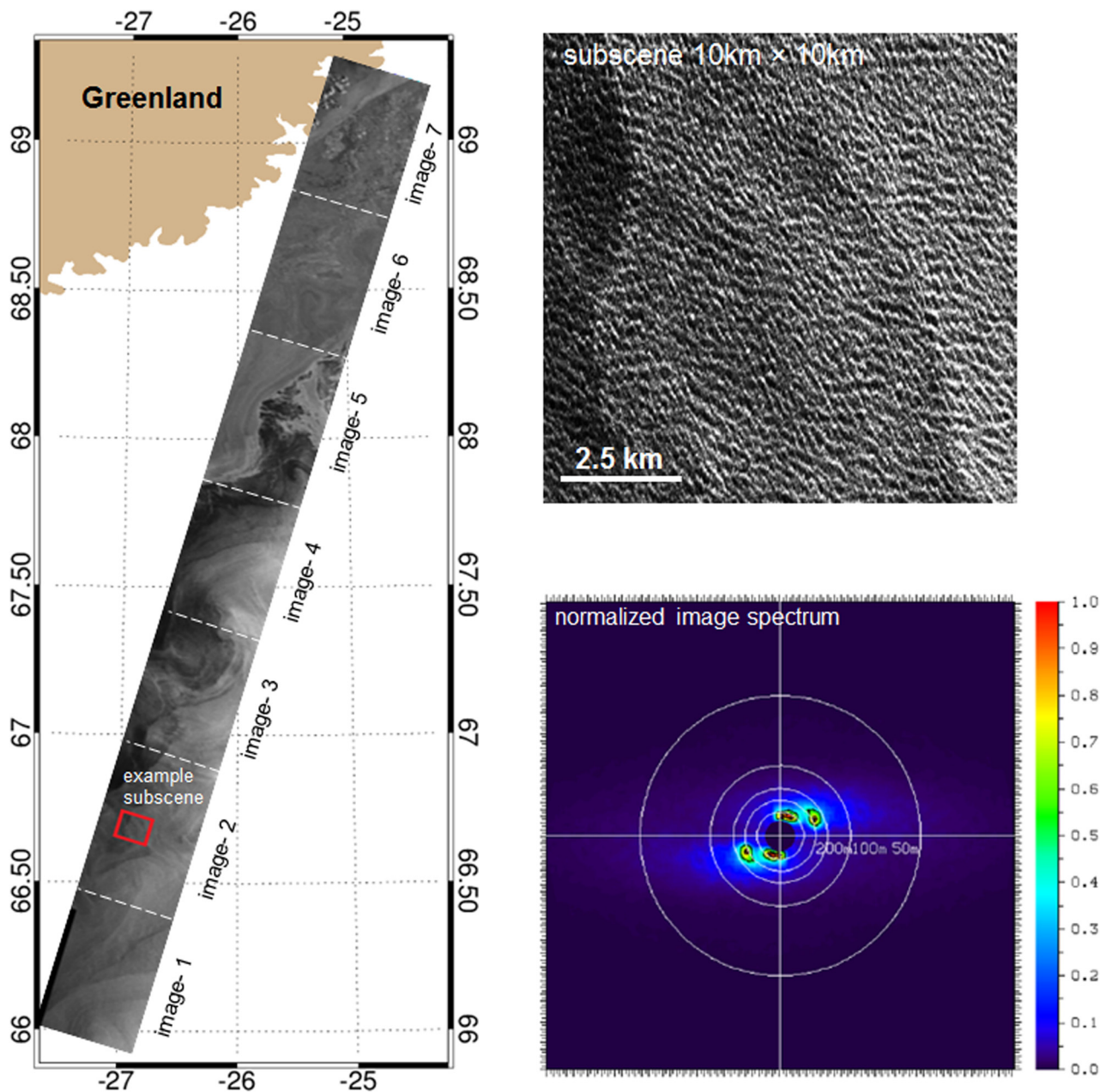

Fig. 1 *Left* TS-X scene made up of seven images in Stripmap mode (30 × 50 km each). The images are numbered from 1 to 7. In image 2, one subscene of ∼10 × 10 km is highlighted by a *red box*. The whole scene is tilted by 16° to 18° with respect to the north-south-direction. *Upper right* An enlargement of the highlighted subscene is shown. *Lower right* Fourier power spectrum of the subscene. Colour scale on the right (the spectrum is normalized with respect to its maximum value). The *white circles* represent the wavelengths of 50, 100, 150, 200 and 300 m. The *white auxiliary line* in vertical direction is the azimuth, i.e. the flight direction of the satellite, and the *white auxiliary line* in horizontal direction is the range direction, i.e. the cross-flight direction. Wavelength larger than 450 m were suppressed by high pass filtering

was subject to two major swell systems: waves of ∼350 m length propagating in the north-north-east to north-east direction through the Denmark Strait, and clearly shorter waves of ∼200 m travelling in west to west-south-west direction. This sea state encounters the MIZ at a significant wave height of around 4 m. The TS-X Stripmap images which are the basis for this investigation are available as a sequence extending from the open ocean to solid ice. The whole scene covers an area of approximately 350 km in the flight direction of the satellite (azimuth) and 30 km in the cross-flight direction (range). Note that a scene length of several hundred kilometres is a major difference with respect to the wave mode imagettes of past and current SAR instruments in space. Peak wavelengths and directions are inferred directly from the image spectra.

This article is organized as follows. In Section 2, an overview on the TS-X satellite is given and the TS-X scene which is the basis for this investigation is introduced. Based on meteorological charts from ECMWF, Section 3 describes the oceanographic and meteorological situation in the area of interest. In Section 4, subsequent data analysis tools based on theoretical properties of water waves are introduced. In Section 5, the methods of retrieving sea state information from TS-X are described. Section 6 comprises both the results and discussion. The findings of this study are summarized in Section 7.

Note that the subsequent Figs. 1, 6, 8, and 9 show images, image subscenes, and/or image spectra from TS-X. For those, the top-to-bottom direction is the azimuth, i.e. flight direction of the satellite, and the right-to-left-direction is the range, i.e. cross-flight-direction. With the flight direction being tilted by 16° to 18° with respect to the north-south-direction, they are not in north-up map orientation. In these figures, relevant geographical positions and orientations are highlighted by an auxiliary map panel.

2 Radar images from the TerraSAR-X satellite

The TerraSAR-X satellite was launched in June 2007 and its normal operation started in January 2008. Its payload is an X-band synthetic aperture radar with a wavelength of 3.1 cm. TS-X acquires images in different modes including ScanSAR, Stripmap and Spotlight. The Stripmap mode has a swath width of 30 km. Compared to some other SAR satellites, TS-X has improved properties against non-linear imaging effects of ocean waves like a reduction of the so called azimuthal cut-off of wavelengths. This is a consequence of the TS-X satellite orbiting at only ∼500 km altitude. The spatial resolution of the TS-X Stripmap mode is close to 3 m. Stripmap images of Multi Look Ground Range Detected (MGD) type have a pixel spacing of 1.25 m. For more details, see http://www.dlr.de/TerraSAR-X.

The basis for this investigation is a TS-X scene consisting of seven satellite images acquired on Feb. 5, 2013 at ca. 8.40 UTC (Fig. 1). All these images were acquired in Stripmap mode (MGD product) and cover an area of 30 × 50 km. From bottom to top, the images are numbered from 1 to 7 and, in the following, the images are referred to by their numbers. Figure 2 shows an ice chart for Feb. 5th, 2013 provided by the Norwegian Meteorological Institute (see http://polarview.met.no/). Therein, the geographical position of the full scene is highlighted. As follows, the TS-X scene starts in the ice-free open ocean and ends at the Greenlandic land mass. In between, the sea ice concentration increases from zero to one.

From the TS-X scene in Fig. 1, different regimes of sea ice are distinguishable. From bottom to top, the TS-X scene is first relatively bright, then exhibits quite dark areas, and becomes brighter again. For the bright parts, scatterers like older rough ice or open water with capillary waves should be present. Because of the lack of capillary waves and its rather smooth surface properties, new and young ice typically appear dark on SAR images (e.g. Wadhams 2002 and references therein). Hence, the dark snake-like band in the TS-X scene, which extends through the images 2 to 5, is deemed to consist of new/young ice. By implication, the brighter areas following north are made up of older ice.

3 The meteo-marine condition

3.1 The large-scale situation

The storm generating the swell waves imaged by TS-X is well represented by operational ECMWF data. Figure 3 shows synoptic weather charts with operational ECMWF data on the mean sea level pressure, wind speed 10 m above sea level and the significant wave height (H_s). These charts are available at a time interval of 6 h. Here, the times of Feb. 3rd, 6 UTC and Feb. 4th, 6 UTC were selected.

On Feb. 3rd, an intensive low-pressure system, with minimum pressure level below 972 hPa, is centred around 56° N and 38° W. In the east to south-east of this low, the winds are southerly to south-westerly generating waves directed towards the acquisition area of the TS-X scene described in Section 2. The maximum significant wave height is around 8 m. The distance between this wave generation area and the acquisition area of the TS-X scene is 1000–2000 km. Wave energy propagates at the wavelength-dependent group speed c_g as described by Eq. 1. Thus, the energy associated with wavelength $\lambda = 350$ m will propagate around 1000 km per day and therefore generated waves of this length will arrive at the acquisition area by the acquisition time.

The low is moving quickly in east-north-east direction and intensifies further. On Feb. 4, the low-pressure system has moved just past the south-eastern part of Iceland. It is now centred at around 11° W and 64° N with minimum pressure below 956 hPa. The strong easterly winds north of Iceland generated the short swell waves that were imaged as well by the TS-X scene a day later.

3.2 At fine temporal and spatial resolution

A sea state hindcast from ECMWF was specifically made for Feb. 5th, 2013, 9 UTC, which practically matches the image acquisition time. The information is summarised in Fig. 4. There, the mean wavelength and wave direction of both wave systems are shown using coloured arrows. The hindcast includes surface currents as black arrows. The significant wave height is given by black contours. The positions of the seven TS-X images are marked by red lines and numbered from 1 to 7. The white to purple shadings are the

sea ice concentration as used by the operational model at the time. Note that the model uses only a coarse representation of the sea ice condition. The sea ice data do not have any ice concentration below 20 % and knowledge of ice characteristics. Also, the parametrisation of the sea-ice effect on the waves is preliminary (Doble and Bidlot 2013), and may not fully represent all interaction processes that might be present. Hence, only the data obtained where is no ice are trusted in the following.

Figure 5 gives a two-dimensional ECMWF wave energy spectrum for Feb. 5th, 2013, 9 UTC, at 26.80° W and 66.68° N (see also the coloured arrows from the ECMWF hindcast in Fig. 4). As expected from the wind in the meteorological charts, the spectrum indicates that the sea state consists of two wave systems. One propagates to the north-north-east at a peak frequency close to 0.075 Hz (roughly 300 m wavelength) and the other one to the west-south-west at a peak frequency close to 0.1 Hz (roughly 200 m wavelength). Other wave systems, like a local wind sea, are neither hindcas-
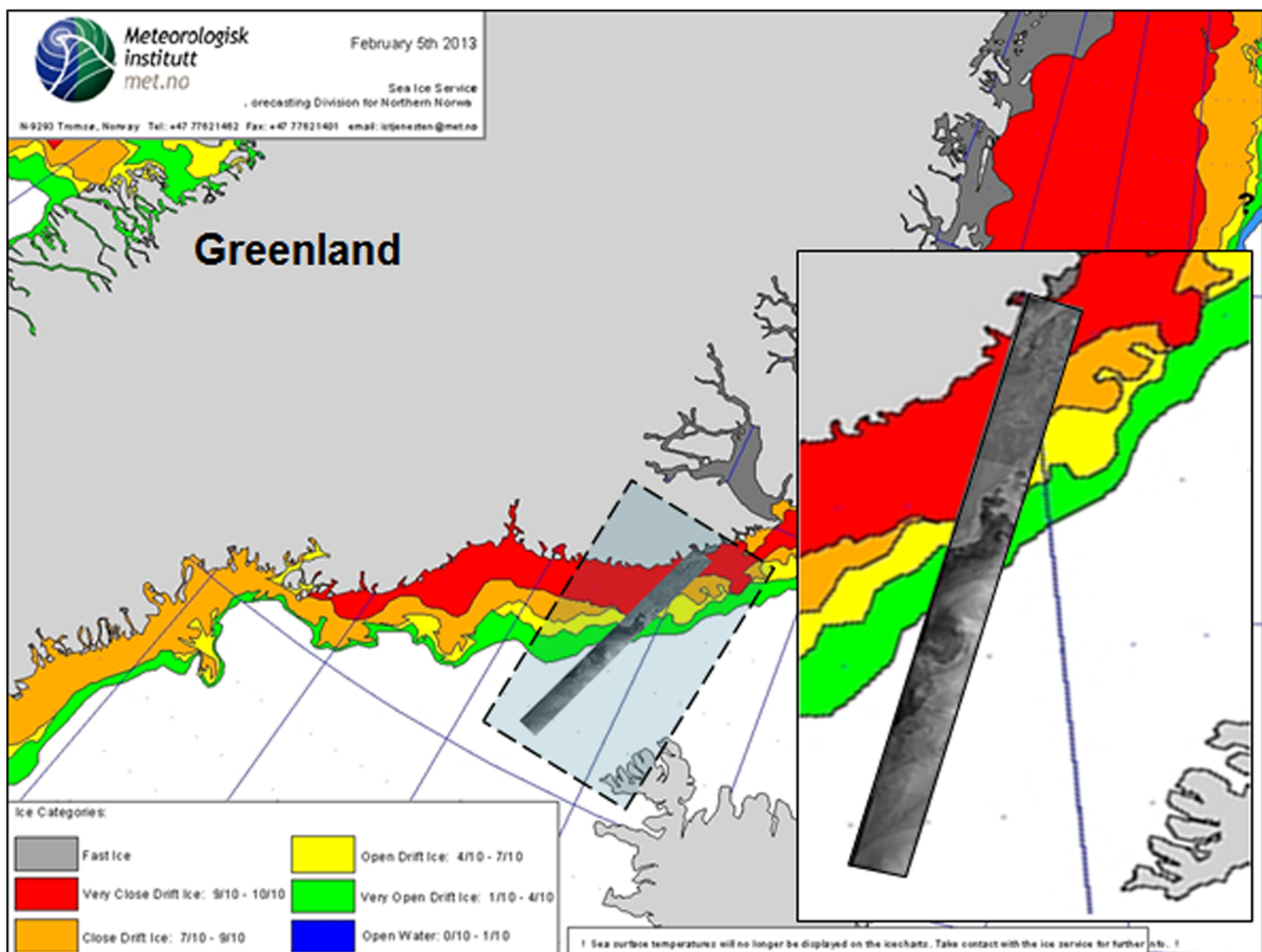

Fig. 2 Ice chart for Feb. 5th, 2013 from the Norwegian Meteorological Institute. The TS-X scene shown in the Figure before is overlaid to the ice chart at its approximate geographical position
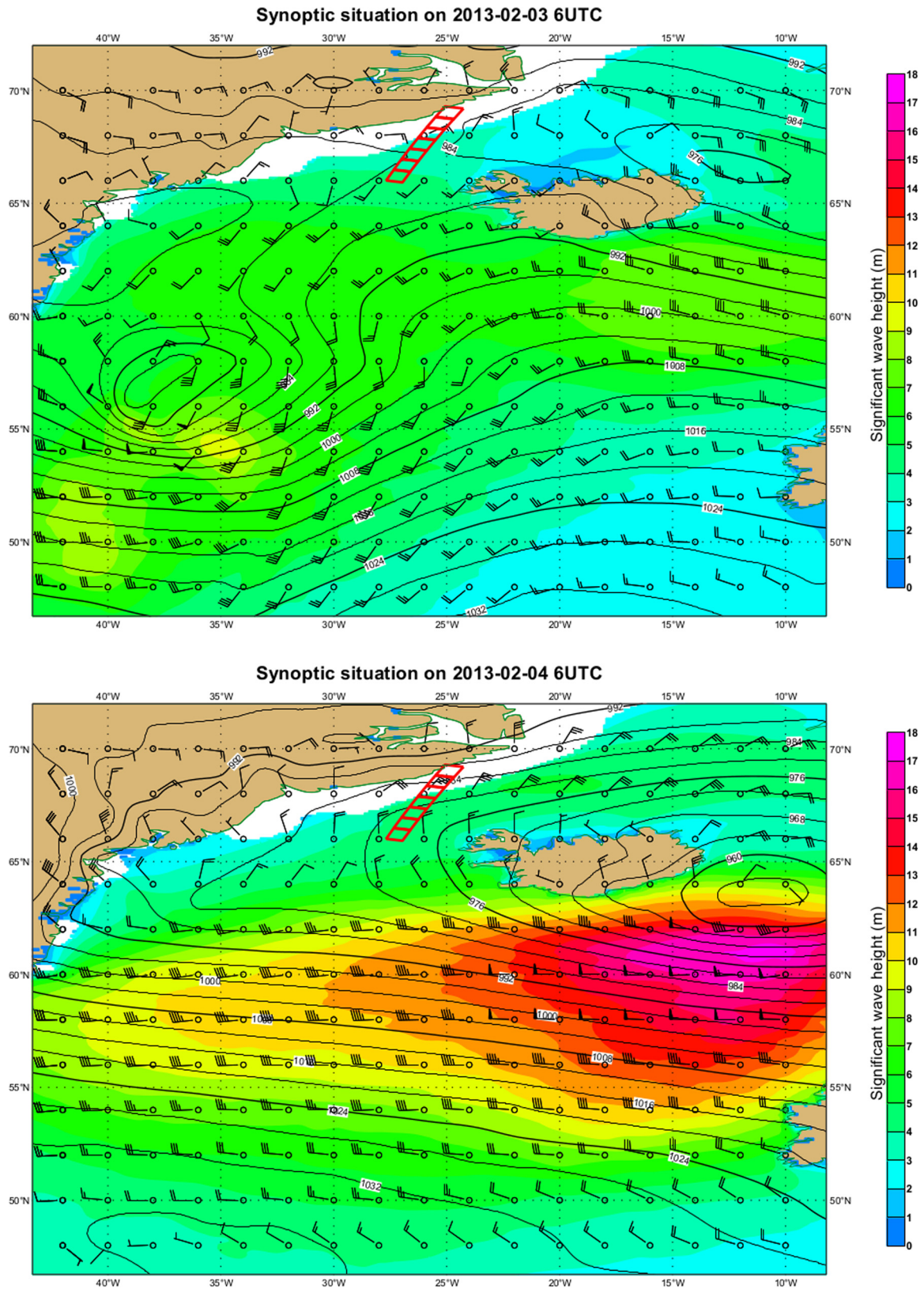
Fig. 3 Synoptic chart for Feb. 3, 6 UTC (*top*) and Feb. 4, 6 UTC (*bottom*) based on operational ECMWF analysis. Data on the mean sea level pressure are given by *black lines*, wind speed 10 m above sea level by *black symbols*, and H_s by coloured contours (colour scale on the *right*). The mean sea level pressure is provided in units of hPa and H_s in units of m. In the chart, the positions of the TS-X images are highlighted by *red boxes*
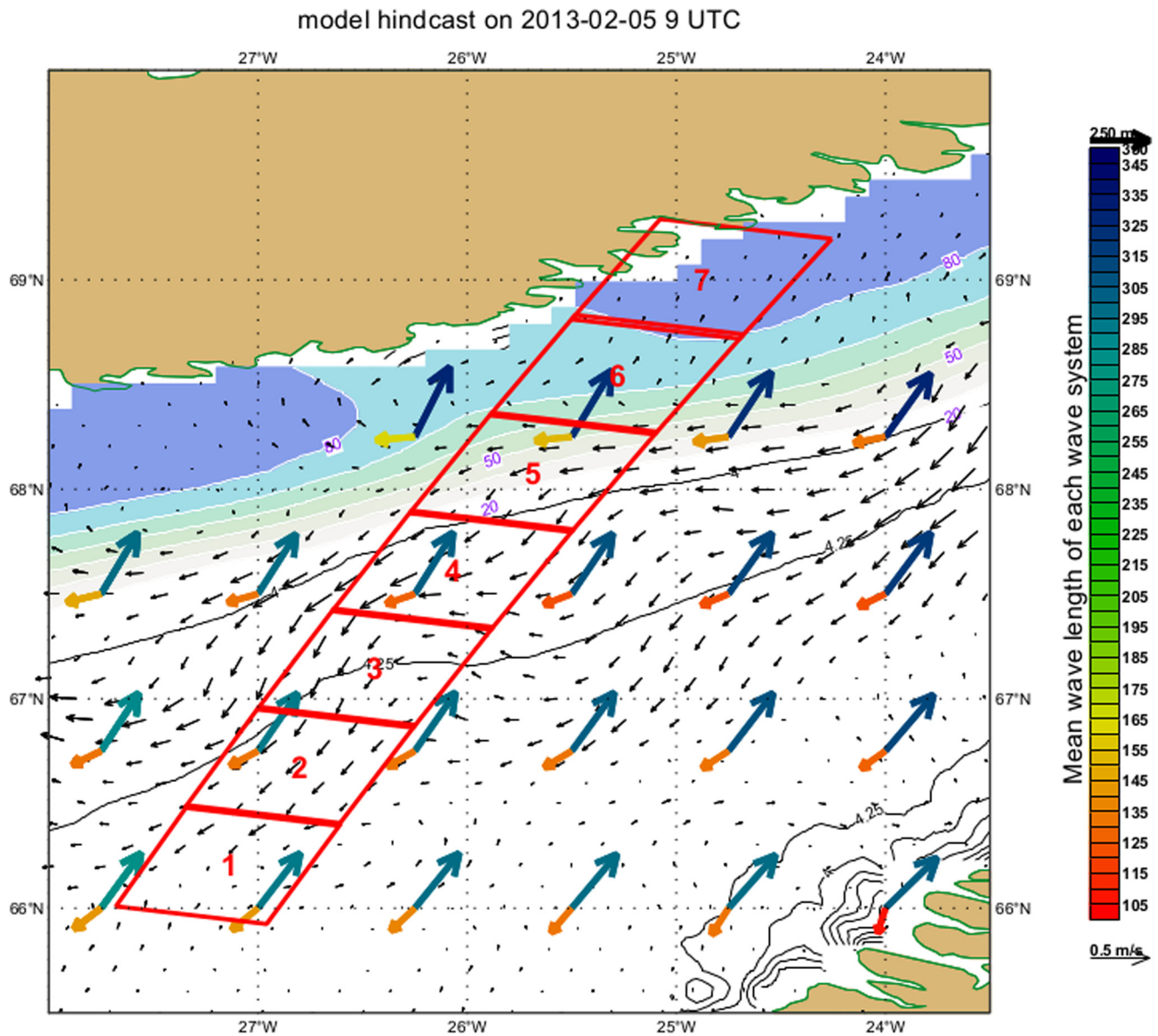
Fig. 4 ECMWF hindcast on the main constituents of the wave field for Feb. 5th, 2013, 9 UTC. The mean wavelength and direction are given by coloured arrows (colour scale on the *right*). The hindcast includes surface currents as provided by the Norwegian TOPAZ4 system, see the *black arrows*. H_s is shown by *black contours*. The positions of the 7 TS-X images are highlighted by *red boxes* and numbered from 1 to 7. The *white to purple shadings* are the sea ice concentration used (only values above 20 % are present)

ted by the ECMWF model nor observed by the TS-X satellite. In addition, ECMWF data indicate the local wind to be low ($<$3–4 ms^{-1}) and of variable direction around the area and time of the satellite image acquisition (not shown here).

4 Wavelength changes due to velocity dispersion

The velocity dispersion being a driver of wavelength variation can be explained as follows. The dispersion relation of

ocean waves in deep water is $\omega^2 = gk$ ($\omega = 2\pi f$ is the angular frequency, f is the wave frequency, $k = \frac{2\pi}{\lambda}$ is the wave number, λ is the wavelength, and g is the gravitational acceleration). The transport of wave energy at the frequency f takes place with the group velocity

$$c_g(f) = \nabla_k \omega = \frac{g}{4\pi f} = \frac{1}{2}\sqrt{\frac{g\lambda}{2\pi}}. \tag{1}$$

The group velocity is frequency/wavelength dependent. Longer wave components move faster. This leads to a sort-

ing of the wave field over time. At a given instance in time, the longer waves have propagated further than the shorter waves. This results in an increasing dominant wavelength in the direction of the wave propagation. The effect of velocity dispersion was extensively analysed for swell across the Pacific by Snodgrass et al. (1966). Measuring at fixed locations, these authors observed a migration of the peak frequency for waves coming from a storm area. For a distance Δ from the storm and a travel time $\tau(f)$, the following relation is given

$$\Delta = c_g(f)\tau(f) = \frac{g\tau(f)}{4\pi f} \qquad (2)$$

or

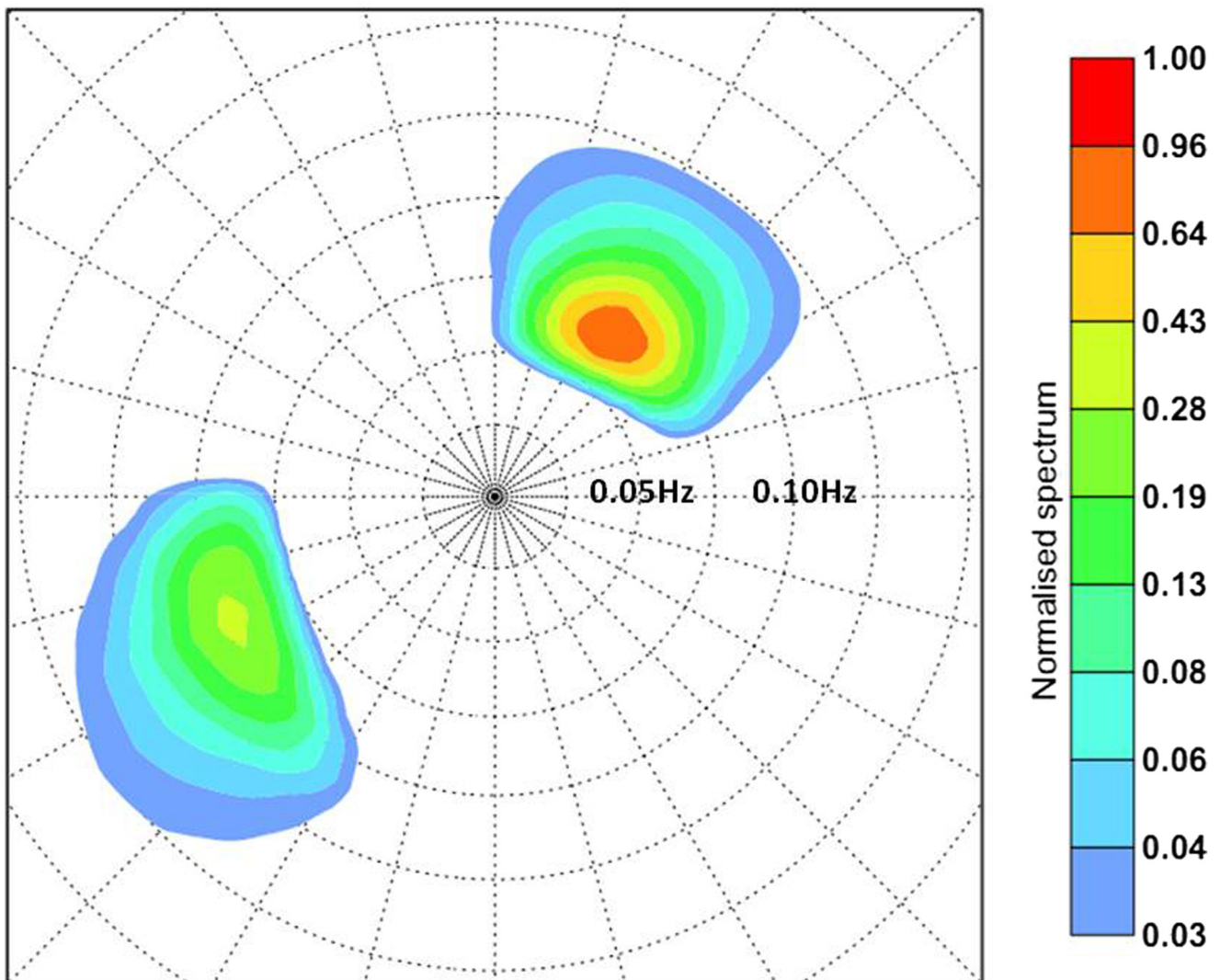$$\frac{df}{d\tau} = \frac{g}{4\pi\Delta}. \qquad (3)$$

Fig. 5 ECMWF wave spectrum for Feb. 5th, 2013, 9 UTC at 26.80° W and 66.68° N, which is in the centre of image 2. The spectrum was normalized by its maximum value. The related H_s value is 4.28 m
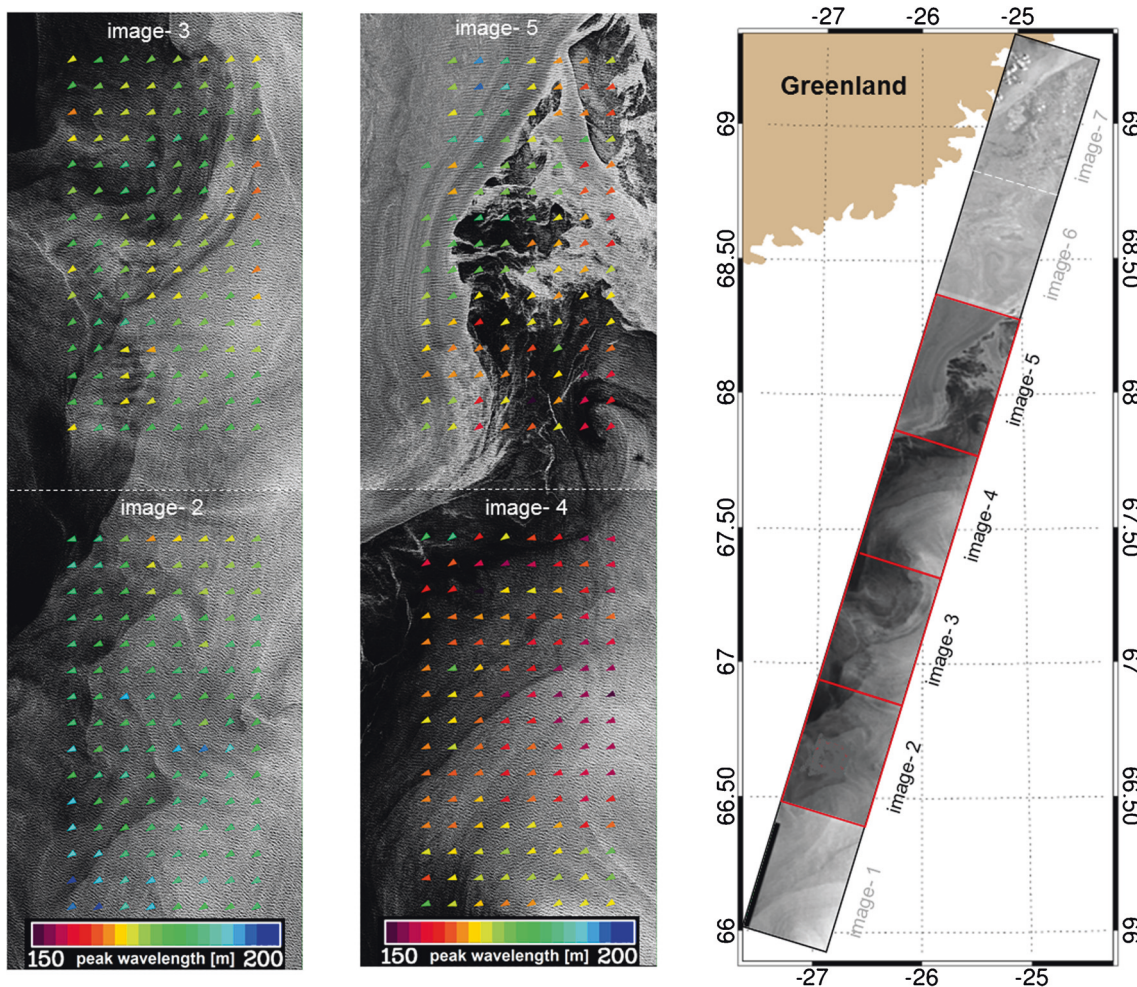
Fig. 6 Peak wavelength and direction of the short swell system (*coloured arrows*), retrieved from the TS-X images 2 and 3 (*left*) and the images 4 and 5 (*middle*). *Right* Position of the utilized TS-X images

A direct consequence of Eq. 3 is that, at a fixed location, the peak frequency grows with time. In a plot of peak frequency against arrival time, the gradient $\frac{df}{d\tau}$ is a function of the storm distance from the location of the measurement. The latter can be compared with meteorological maps.

This analysis concept needs some modification for being applied to SAR images of ocean waves, from which the spatial pattern of the peak wavelength λ is determined as described in Section 5.1. Being a snapshot at one point in time rather than a time series, the wave travel time τ is assumed to be constant over one SAR image. The peak frequency decreases into the travel direction of waves or, equivalently, the peak wavelength increases, i.e. $\frac{d\Delta}{d\lambda} > 0$. With $\Delta = c_g \tau$ and $\tau = $ constant, we obtain

$$\frac{d\Delta}{d\lambda} = \frac{dc_g}{d\lambda}\tau = \frac{dc_g}{d\lambda}\frac{\Delta}{c_g}. \tag{4}$$

Eq. 1 implies that

$$\frac{dc_g}{d\lambda} = \frac{1}{4}\left(\frac{g}{2\pi}\right)^{0.5}(\lambda)^{-0.5} \tag{5}$$

and

$$\frac{1}{c_g}\frac{dc_g}{d\lambda} = \frac{1}{2\lambda}. \tag{6}$$

Inserting this into Eq. 4 yields

$$\Delta = 2\lambda\frac{d\Delta}{d\lambda}. \tag{7}$$

Since Δ and λ are positive quantities, the gradient $\frac{d\Delta}{d\lambda}$ is positive as well. This means that the wavelength grows in propagation direction for the condition of swell in the open ocean.

As described before, the long swell imaged by TS-X has a wavelength of $\sim$350 m and a travelling distance of $\sim$2000 km. Following (7), the corresponding rate of

wavelength increase is around 0.35 m per km. This corresponds with an overall increase of wavelength of a few meters within one single TS-X image of 30×50 km in area.

5 Sea state retrieval from TerraSAR-X

5.1 Peak wavelength and direction

The sea state is retrieved from TS-X images by applying two-dimensional fast Fourier transformation (FFT) to selected subscenes of approximately 10×10 km. This subscene size ensures an appropriate resolution in the wave number space. Note that the FFT resolution in k-space is given by $\frac{2\pi}{L}$ with L being the subscene length. Thus, even the long swell waves present in the TS-X scene are resolved better than 15 m in the wavelength space. The peak wavelength and direction are directly inferred from the wavenumber and direction of the maximum of the Fourier power spectra. This is based on the assumption of a linear relationship between the image and wave spectra. The validity of this approach has been proven in Bruck and und Lehner (2012). It is worth while noting that non-linear imaging effects of SAR instruments are, in principle, reduced in ice by the absence of very short and random water waves (e.g. Schulz-Stellenfleth and Lehner 2002). This is because of the orbital velocity of these waves giving rise to the so-called azimuthal cut-off of waves.

In Fig. 1, one subscene of image 2 is shown enlarged and its FFT power spectrum is provided. In the spectrum, different peaks are evident, one at more than 300-m wavelength and the other one short below 200-m wavelength (both maxima appear twice due to the 180° ambiguity inherent in the Fourier spectra). This indicates the presence of two systems of waves. These are consistent with the system of long and short swell shown by ECMWF data as described in Section 3.2. Besides, the latter sufficiently resolves the aforementioned 180° ambiguity in the example Fourier spectrum from satellite.

For image 2 to 5, curves of the arithmetic means of the peak wavelength and direction are provided in Fig. 7. The long swell data were averaged in range, i.e. cross-flight direction of the satellite, and the short swell data in azimuth, i.e. flight direction of the satellite. The resulting peak wavelengths are discussed in detail in Section 6.1. The resulting peak wave directions are between north-north-east and north-east for the long swell and between west-south-west and west for the short swell.

5.2 Significant wave height

The XWAVE algorithm for determining H_s from TS-X images is described in Bruck and und Lehner (2012).

The XWAVE retrieval is based on an empirical relation between H_s and spectral and wind parameters. Meanwhile, a more recent version of XWAVE accounting for several not directly sea-state related spectral features is available (Pleskachevsky et al. 2016). It is used here. Note that this algorithm is designed for use in open and coastal waters. Although an inhomogeneous ice cover may partly resemble the complex features of a coastal region, the algorithm has not been validated under ice conditions so far.

In the ice-free open ocean, the satellite data on H_s have values in the range from 3 to 4 m, e.g. large parts of image 1. This is consistent with the H_s values from the ECMWF hindcast (Figs. 4 and 5). For reasons of algorithm design, any H_s values in the ice-infested region of the TS-X scene cannot be considered scientifically conclusive and are omitted here. Similarly, the wave heights in ice from ECMWF are limited by the coarse ice representation of the model, pointed out in Section 3.2.

6 Results and discussion

6.1 Spatial variation of wavelength

The retrieval of significant wave height from TS-X images is based on empirical algorithms and so far its robustness has only been proven in ice-free water. However, the retrieval of peak wavelength and direction is a direct method, valid independent of the presence of ice. In the following, we will discuss the evolution of wavelength as the waves propagate into the MIZ.

From the ECMWF hindcast, a wavelength increase in the wave propagation direction becomes visible for both swell wave systems, see Fig. 4. A plausible explanation for this behaviour is offered by the velocity dispersion of waves. As described in Section 4, the longer the waves, the faster they travel. Of course, another potential factor influencing the wavelength is the interaction between waves and currents. As follows from the current data from ECMWF in Fig. 4, the surface current off the coast of Eastern Greenland is not very strong, but has certain gradients. Running the ECMWF hindcast with and without currents, it was concluded that current-related modulation of wavelength may account for few meters at most. Moreover, its spatial pattern is quite irregular because of the correlation with mesoscale features of ocean currents. Thus, currents cannot explain the gradual increase of wavelength with travelling direction evidenced above.

The images 2 to 5 from TS-X are provided in combination with coloured arrows representing resulting peak wavelengths and directions in Fig. 6. For any of the images, the arrows follow a raster-like pattern with steps of 3000 m
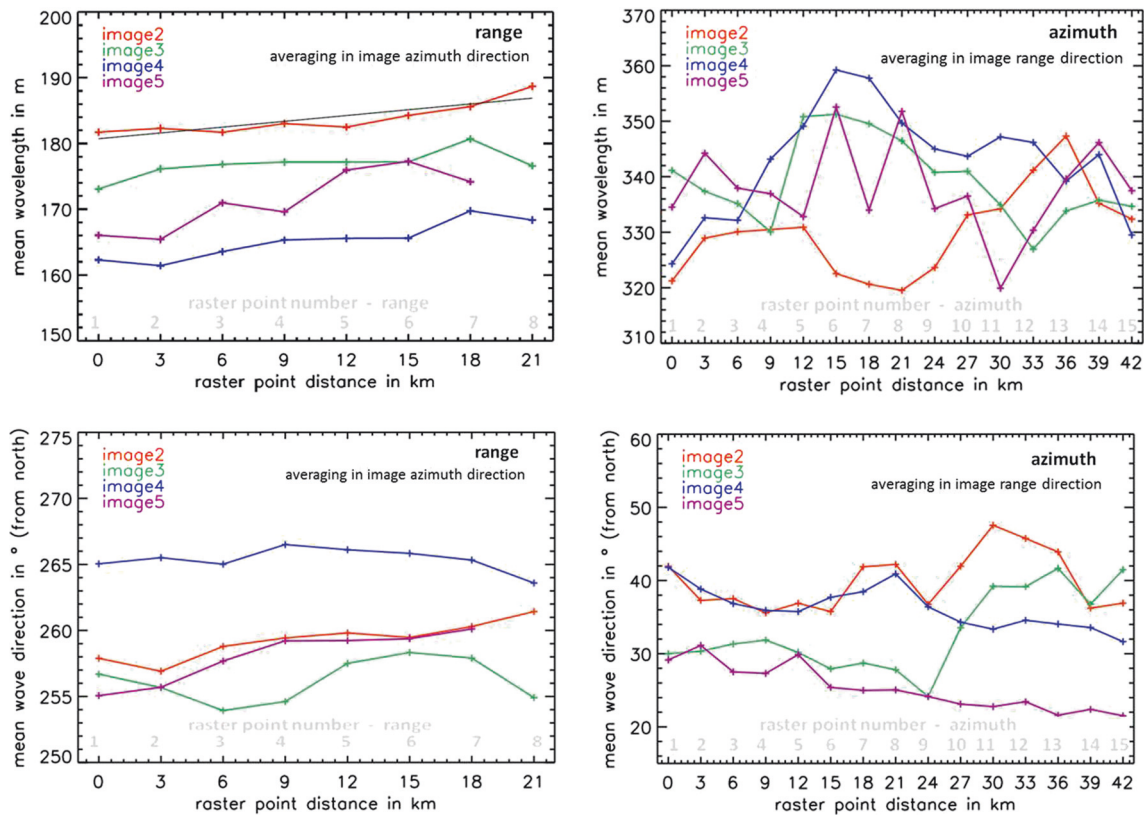
Fig. 7 Spatial distribution of the mean values of peak wavelength (*top*) and direction (*bottom*), retrieved from the TS-X images 2 to 5. *Left* are the peak wavelength and direction of the short swell system and *right* those of the long swell system

between adjacent arrows. The arrow colour is indicative of the value of wavelength, and the arrows point into the wave travelling direction. Each arrow is centred within the related subscene of ∼10×10 km. A colour scale comprising wavelengths in the 150–200 m range is added at the bottom of the figure. Note that this analysis was restricted to the short swell waves.

The wavelengths from image 2 to 5 have as well the tendency to increase in wave propagation direction. A comprehensive illustration of this fact is given in Fig. 7, upper left panel. There, the data of peak wavelength were averaged image by image over the 15 azimuthal raster points. With the primary raster pattern of data having altogether eight columns per image, each image is represented by a curve comprising eight points. They are ordered in right-to-left image direction. The argument on the x-axis is the raster point distance in km. For image 5, the last point was omitted with the short swell becoming partly undetectable at the left edge of the image. As follows, the peak wavelength has the tendency to increase in right-to-left image direction (and hence, into the wave propagation direction which differs in average by 20° to 30° from that).

In Fig. 7, upper left panel the curve for image 2 is plotted together with a linear fitting curve. The latter was determined by linear regression with the autocorrelation of consecutive curve points being taken into account by Cochrane-Orcutt transformation (Cochrane and Orcutt 1949). This autocorrelation may arise from neighbouring FFT-analysed subscenes of TS-X having a certain overlap. The regression line has a slope or gradient of 0.33 ± 0.07 m/km. Its uncertainty is the 1σ value calculated from the covariance matrix of regression. The latter is based on the fit residuals, i.e. the difference between the curve and its regression line. Both the slope and its uncertainty were projected from the right-to-left image direction onto the average wave direction along the curve for image 2. This projection was done by dividing the value of slope and uncertainty, which primarily results from the regression, by the cosine of the angle difference between these two directions. The average wave direction along the curve deviates by 27° to the left from the right-to-left image direction (not shown here, but consistent with image 2 in Fig. 6). Subsequently, the inverse value of the slope was used as $\frac{d\Delta}{d\lambda}$ in Eq. 7. The average wavelength along the curve for image 2, which is

184 m, was used as λ. This yields an estimated distance to the wave generation area of 1110 ± 247 km. The uncertainty of the slope, resulting from regression, was converted into the uncertainty of the estimated distance via first-order Taylor-approximation.

The estimates of the distance to the wave generation area are provided for image 2 to 5 in Table 1. They were calculated analogously. The largest value is 1522 ± 387 km, for image 3, and the smallest value is 436 ± 66 km, for image 5. By order of magnitude, these estimates match the travelling distance expected for the short swell waves as described below. Thus, the velocity dispersion similarly offers a plausible explanation for the wavelength increase evident from the TS-X images.

A minimum value of the travelling distance of the short swell can be estimated as follows. In Fig. 6, image 1 was omitted because of the absence of the short swell. The latter is demonstrated in Fig. 8 calculating a cross spectrum from complex SAR data. The most likely explanation for this is given by geographical constraints. With the travel direction of waves having a strong east-to-west component, the wave system has been blocked by the landmass of Iceland. The Vestfirdir Peninsula (also known as the Westfjords) is that part of the main island of Iceland which is nearest to the acquisition area of image 1. With the geographical position of the Peninsula represented by 65° 44′ 15″ N and 22° 10′ 14″ W and the centre coordinates of image 1 being given by 66° 12′ 35″ N and 27° 8′ 27″ W, the loxodromic distance between both is around 230 km.

Another feature is that the increase rate of wavelength varies from image to image in Fig. 7. This favours other sources of wavelength variability being overlaid to the presumably dispersion related wavelength increase. The increase rate grows from image 3 to 5. This points towards the possibility of the wavelength increase being even enhanced in ice. For this, in turn, one potential explanation arises from the selective attenuation of high wave frequency, or low wavelength, respectively, by sea ice. A basic description of this selective attenuation was given in Wadhams et al. (1986) and Wadhams et al. (1988). Besides, elasticity models offer a theoretical approach which is able to predict the wavelength to increase in ice with respect to open water (Squire et al. 1995).

The variation of the long swell wavelength is similarly shown in the upper right panel of Fig. 7. The data of peak wavelength were averaged image by image over the range direction. With the primary raster pattern of data having altogether 15 points in the azimuthal direction, each image is represented by a curve comprising 15 points. They are ordered in bottom-to-top image direction. In general, the long swell wavelength exhibits considerable irregularity. Nevertheless, the curve for image 2 increases linearly between the second and fifth curve point at a

rate of around 0.2 to 0.3 m/km. In addition, the 10th, 11th and 14th curve point are a prolongation of the rather straight increase between the 2nd and 5th curve point. The observed increase rate is consistent with the long swell waves having travelled a distance of 2000 to 3000 km (practically consistent with Section 3.1). This follows from inserting the inverse value of the increase rate given above as $\frac{d\Delta}{d\lambda}$ into Eq. 7 and using a value of around 350 m for λ.

6.2 On the penetration of the waves into the ice

In the upper left corner of image 4, the boundary between new/young and older ice is reached as follows from the transition from dark to brighter radar cross section σ_0 (see e.g. image 4 in Fig. 6). After passing through the edge of the dark appearance of the young ice, the waves disappear relatively quickly below detectability in the following TS-X images. In image 5, the waves are still identifiable throughout the largest part. In image 6, wave patterns are only present in the lower and right part. The latter is indicated by the peak wavelengths presented in the upper right panel of Fig. 9. The values of peak wavelength, resulting after FFT from the image power spectra, not exceeding 400 m may serve as criterion for the presence of the long swell in the SAR scene. Tests have shown that the peak wavelengths of the long swell are typically below ∼380 m in our case. Due to spectral leakage effects, image texture from ice typically confounds with larger wavelength. Excluding wavelengths greater than 400 m is largely consistent with restricting to those image portions with the pattern of long swell being visible to the eye.

A detailed view on where the short and long swell terminate in the ice is given in Fig. 9. In the lower right panel, image 6 is shown with some subscene of ∼10 × 10 km being enlarged. For the largest part of this subscene, the waves encounter older ice. Some dark colour typical for new/young ice only appears at the outermost edge of the subscene in the lower right part. It is evident that the wave pattern terminates in the subscene. Both the short and long swell are visible in the lower right part of the subscene. There, the overlay of the long and short swell results in wave fronts being imaged as wiggles. As described by Ardhuin et al. (2015), this effect is typical in ice. Differently, the wave fronts appear as straight lines some kilometres deeper in the ice. By implication, the long swell is the only remaining wave system there. In the upper left part of the subscene, the long swell has vanished as well. In addition, the bottom of Fig. 9 shows image 6 overlaid by data on the long and short swell wavelength. The data are organised into the same raster pattern as before. The long swell wavelengths were filtered by the above described criterion. For the short swell, the peak wavelength not exceeding 175 m was used as

Table 1 For image 2 to 5, the table provides the whole-image-average of the wave propagation direction (relative to the right-to-left image direction), the whole-image-average of the wavelength, the slope of the regression line projected onto the whole-image-average wave direction and the estimated distance to the wave generation area

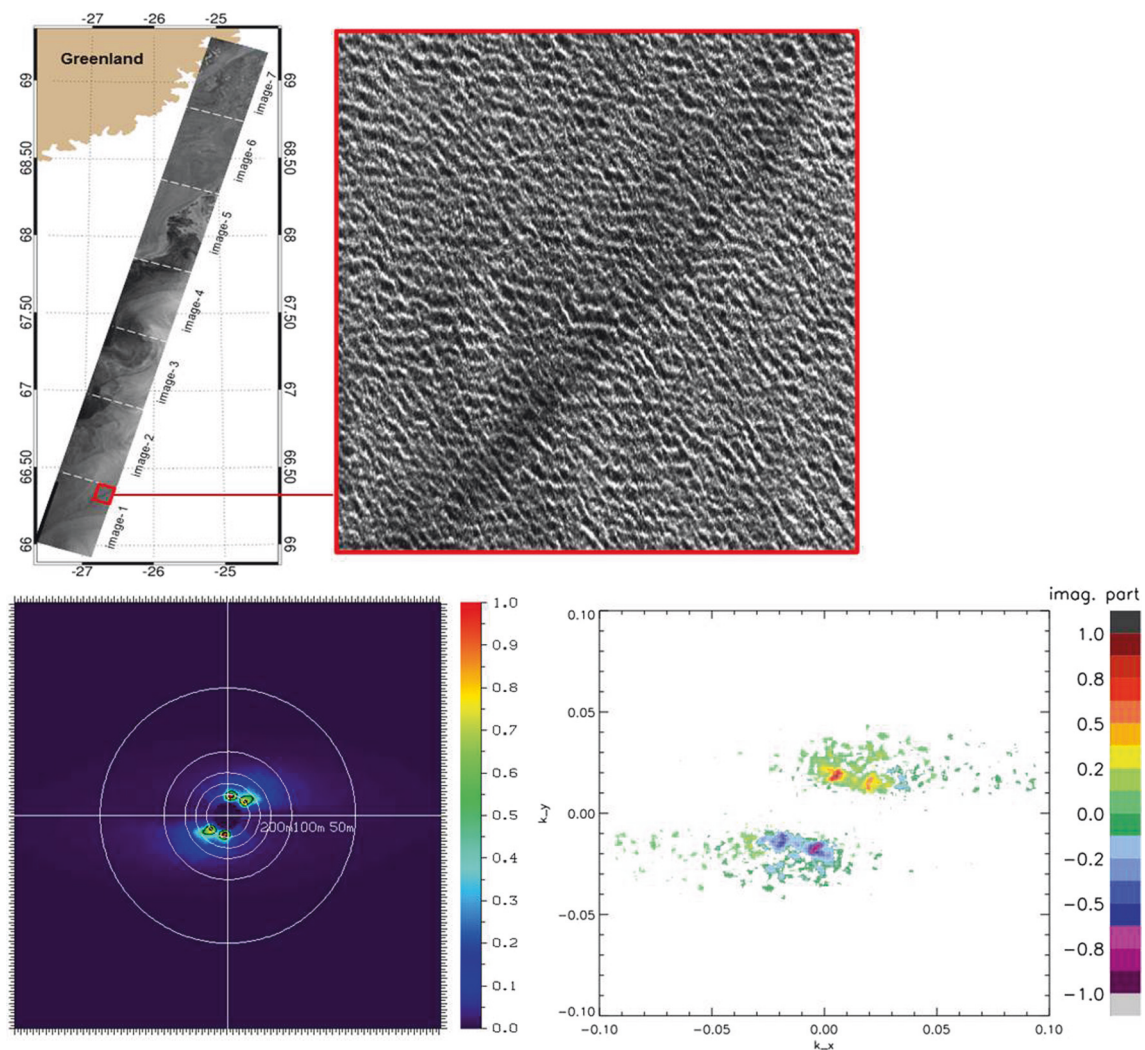| 5	4	3	2	Image number
29	22	31	27	Average wave direction in units of °
171	165	177	184	Average wavelength in units of m
0.79 ± 0.12	0.41 ± 0.03	0.23 ± 0.06	0.33 ± 0.07	Slope of the regression line in m/km
436 ± 66	803 ± 68	1522 ± 387	1110 ± 247	Estimated distance to the wave generation area in km

These numbers are specifically for the short swell

Fig. 8 In the *upper left*, the TS-X scene is shown with one subscene of image 1 highlighted by a *red box*. The area of the subscene is ~10 × 10 km. In the *upper middle*, this subscene is shown enlarged. In the *lower left*, the image spectrum of the subscene is provided. As in Fig. 1, this spectrum was calculated from intensity SAR image and has a 180° ambiguity. In the *lower right*, the imaginary part of the cross spectrum of the subscene is shown. The cross spectrum was calculated from the complex image 1. The x-axis / y-axis shows the x-component / y-component of the wave number vector. Only those parts of the spectrum with absolute imaginary values larger than 0.05 are plotted, the rest remains blank. The cross spectrum is consistent with the intensity spectrum. The positive values of the cross spectrum indicate the actual travelling direction of waves, which is predominantly to the north and east. Detailed information on the calculation of SAR cross spectra can be found in Schulz-Stellenfleth and Lehner (2002 and references therein)
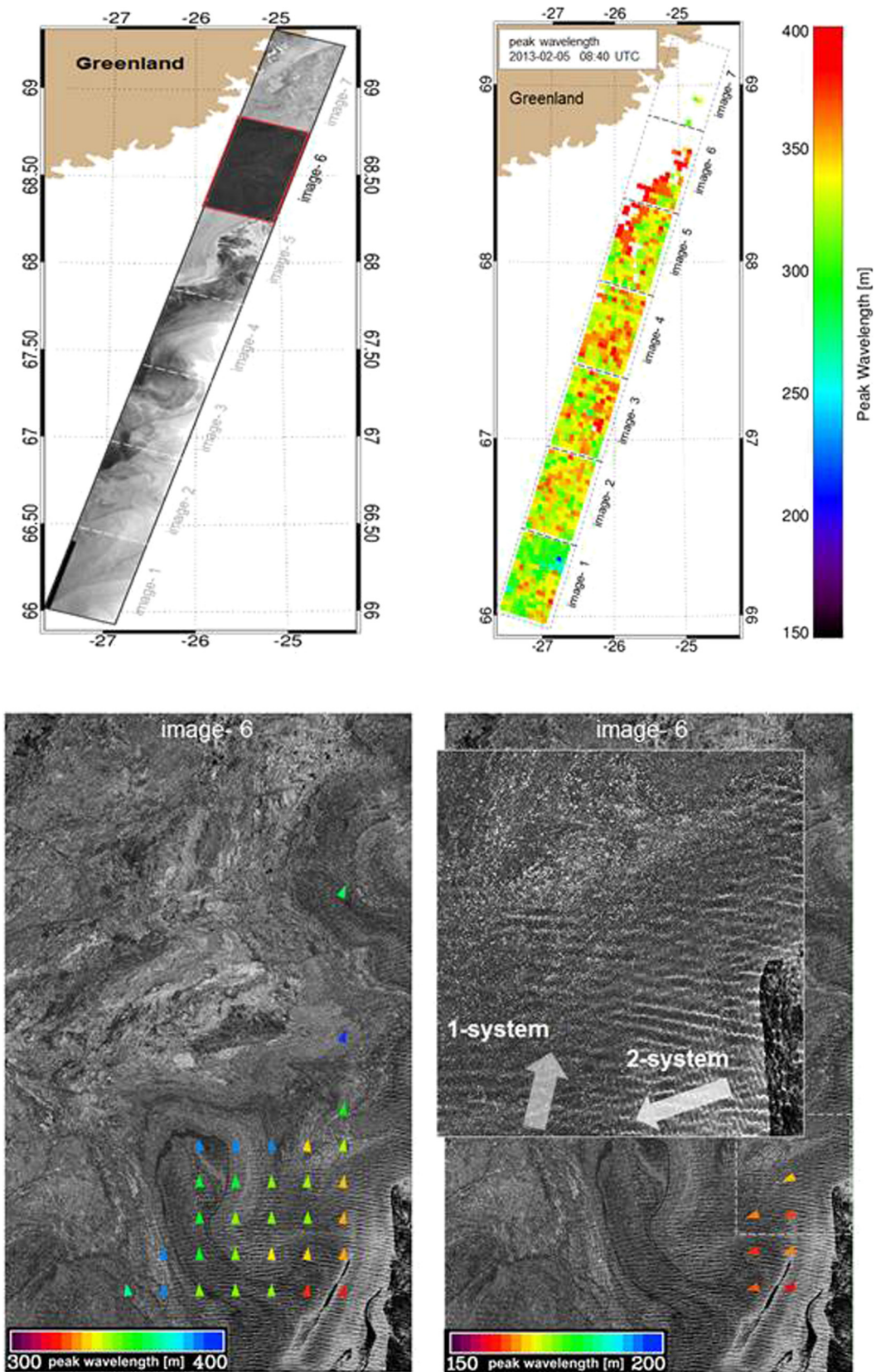
Fig. 9 *Top* The geographical position of the TS-X scene is shown with image 6 being highlighted (*left*). The results on the long swell wavelength over the full TS-X scene (*right*). *Bottom* Image 6 is provided with one subscene of ∼10 × 10 km enlarged. Image 6 is overlaid by data on the long swell wavelength (*left*) and short swell wavelength (*right*)

filter criterion. This is practically equivalent with confining to those image portions with the short swell waves being visible to the eye. It follows that the long swell waves penetrate somewhat deeper into the ice than the short ones.

7 Summary and conclusion

A sea state event in the MIZ has been analysed from a Stripmap scene acquired by the TerraSAR-X satellite on Feb. 5th, 2013 off the coast of Eastern Greenland. Two systems of swell waves, a long swell of ∼350 m length and a shorter swell of 150–180 m length, have been identified to penetrate deeply into the MIZ. In the TS-X scene, the waves start from the ice free open ocean and subsequently encounter ice types of different stage.

The overall penetration of waves into the ice evidenced here has similarity to Ardhuin et al. (2015) reporting that swell waves in the MIZ decayed exponentially over a distance on the order of 200 km. In older ice, we observed both wave systems falling below detectability over a distance of a few tens of kilometres. The long swell waves are detectable somewhat deeper into the ice than the short swell waves. This is reminiscent of the finding that even the damping of long swell has an e-folding distance of a few tens of kilometres in ice floe condition, summarised in Wadhams et al. (1988) and Schulz-Stellenfleth and Lehner (2002). The e-folding distance becomes somewhat larger for increasing wavelength.

For both swell wave systems observed by TS-X, operational ECMWF data indicate the passage of a storm in the Atlantic to be the origin. An ECMWF model hindcast was made specifically for the time of the satellite image acquisition. The hindcast confirms a sea state pattern consisting of a longer and shorter system of swell waves around the image acquisition area. Moreover, the hindcast data exhibit an increase of wavelength into the travel direction of both swells. For each of the wave systems, the velocity dispersion of ocean waves offers a plausible explanation for the increasing behaviour. Similar increases of the short swell wavelength into the wave travel direction were evidenced within the images 2 to 5 from TS-X. The rate of increase is consistent with the expected distance to the wave generation area. Still, the rate of increase varies from image to image. This points towards sources of variability other than wave dispersion being overlaid. For image 5, the strongest increase was obtained. Possibly, the open-water increase of wavelength was enhanced by wave-ice-interaction.

References

Ardhuin F, Collard F, Chapron B, Girard-Ardhuin F, Guitton G, Mouche A, Stopa JE (2015) Estimates of ocean wave heights and attenuation in sea ice using the SAR wave mode on Sentinel-1A. Geophys Res Lett 42. doi:10.1002/2014GL062940

Bruck M, und Lehner S (2012) Sea state measurements using TerraSAR-X data. In: Proceedings of IGARSS 2012, IEEE Press, pp 7609–7612

Cochrane D, Orcutt GH (1949) Application of least squares re- gression to relationships containing autocorrelated error terms. J Amer Stat Assoc 44:32–61

Doble MJ, Bidlot J-R (2013) Wave buoy measurements at the Antarctic sea ice edge compared with an enhanced ECMWF WAM: progress towards global waves-in-ice modelling. Ocean Modell 70:166–173

Doble M, De Carolis G, Meylan MH, Bidlot J, Wadhams P (2015) Relating wave attenuation to pancake ice thickness, using field measurements and model results. Geophys Res Lett. doi:10.1002/2015GL063628

Kohout AL, Williams MJM, Dean S, Meylan MH (2014) Storm-induced sea ice breakup and the implications for ice extent. Nature 509:604–607

Pleskachevsky A, Rosenthal W, Lehner S (2016) Meteo-marine parameters for highly variable environment in coastal regions from satellite radar images, ISPRS J Photogram Remote Sens. doi:10.1016/j.isprsjprs.2016.02.001

Schulz-Stellenfleth J, Lehner S (2002) Spaceborne synthetic aperture radar observations of ocean waves traveling into sea ice. J Geophys Res 107(C8):3106. doi:10.1029/2001JC000837

Snodgrass FE, Groves GW, Hasselmann KF, Miller GR, Munk WH, Powers WH (1966) Propagation of ocean swell across the Pacific. Phil Trans R Soc Lond A 259:431–497. doi:10.1098/rsta.1966.0022

Squire V, Dugan J, Wadhams P, Rottier P, Liu A (1995) Of ocean waves and sea ice. Annu Rev Fluid Mech 27(3):115–168

Squire VA (2007) Of ocean waves and sea-ice revisited. Cold Reg Sci Technol 49(2):110–133. doi:10.1016/j.coldregions.2007.04.007

Wadhams P, Squire VA, Ewing JA, Pascal RW (1986) The effect of the marginal ice zone on the directional wave spectrum of the ocean. J Phys Oceanogr 16(2):358–376

Wadhams P, Squire VA, Goodman DJ, Cowan AM, Moore SC (1988) The attenuation rates of ocean waves in the marginal ice zone. J Geophys Res 93(C6):6799–6818. doi:10.1029/JC093iC06p06799

Wadhams P, Parmiggiani FE, de Carolis G (2002) The use of SAR to measure ocean wave dispersion in frazilpancake icefields. J Phys Oceanogr 32(6):1721–1746

Wadhams P, Parmiggiani FE, de Carolis G, Desiderio D, Doble MJ (2004) SAR imaging of wave dispersion in Antarctic pancake ice and its use in measuring ice thickness. Geophys Res Lett 31. doi:10.1029/2004GL020340